HTML ABSTRACT • LINKS

Intersubband absorption of strain-compensated $Si_{1-x}Ge_x$ valence-band quantum wells with $0.7 \leq x \leq 0.85$

T. Fromherz,[a] M. Meduňa,[b] and G. Bauer
Institut für Halbleiter- und Festkörperphysik, Universität Linz, A-4040 Linz, Austria

A. Borak, C. V. Falub, S. Tsujino, H. Sigg, and D. Grützmacher
Paul Scherrer Institut, 5232 Villigen PSI, Switzerland

(Received 9 March 2005; accepted 21 June 2005; published online 16 August 2005)

Strain-compensated, *p*-type SiGe quantum wells with a high Ge concentration of up to 85% have been grown on commercially available $Si_{0.5}Ge_{0.5}$ pseudosubstrates by molecular-beam epitaxy. Structural investigations by transmission electron microscopy and high-resolution x-ray reflection and diffraction showed that at a growth temperature around $T=300$ °C, samples in excellent compliance with the design parameters, comparatively sharp interfaces, and negligible increase of growth-induced surface roughness can be grown. Comparison of polarization-dependent intersubband absorption measurements with simulated intersubband absorption spectra shows that for the quantum wells investigated in this work, the hole eigenstates, their in-plane dispersion, and the polarization-dependent intersubband transition matrix elements are accurately described by a strain-dependent, six-band $\mathbf{k}\cdot\mathbf{p}$ Luttinger-Kohn Hamiltonian in which only one fitting parameter—the intersubband transition linewidth—is used. © *2005 American Institute of Physics*.
[DOI: 10.1063/1.1997292]

I. INTRODUCTION

Due to its indirect fundamental band gap in *k* space, bulk silicon—the dominating material for microelectronics—is not suitable for optoelectronic applications. However, since the processing technology is highly developed for this material system and a potential monolithic integration of electronic and optical devices would further enhance the application potential of Si, many strategies have been proposed and developed in order to add optoelectronic performance to the Si material system. Most of these strategies rely on the relaxation of the *k*-space selection rules for optical transitions by spatial localization of holes and/or electrons. The most prominent among them are the confinement of carriers in $Si_{1-x}Ge_x$ quantum wells (QWs) and dots (QDs),[1] by strain fields in highly boron-doped layers,[2,3] in porous Si,[4–6] and in Si nanocrystals.[7,8] From the technological point of view, the use of $Si_{1-x}Ge_x$ QWs is the most developed approach that is nowadays employed in many commercially available integrated circuits in order to enhance the maximum allowable frequency.

For optoelectronic applications SiGe QWs have been used in quantum well infrared photodetectors[9,10] (QWIPs) and in cascade emitters.[11–15] However, if SiGe QWs are grown on Si substrates, misfit strain due to the larger lattice constant of SiGe limits the maximum thickness of the devices. Therefore, in order to grow the large number of QWs that are necessary to achieve, for example, sufficient gain in SiGe cascade structures, strain-compensated structures have to be designed on SiGe pseudosubstrates. Such substrates consist of a relaxed SiGe buffer with a Ge concentration ramped up from 0% to, for example, 50% followed by a layer with constant Ge concentration. In these buffers the misfit dislocations are confined to the grading region, leaving the buffer part with constant Ge concentration virtually defect free. Such pseudosubstrates are commercially available and the growth of up to 30 periods of a SiGe cascade emitter structure on these substrates has been demonstrated recently.[12]

II. SAMPLE GROWTH AND PREPARATION

In order to optimize the growth of SiGe QWs and the theoretical models describing the intersubband transitions in such complicated cascade structures, in this work simple QW structures on commercially available $Si_{0.5}Ge_{0.5}$ pseudosubstrates have been designed. These substrates consist of a several micrometer thick layer in which the Ge content is ramped up from 0% to 50% and a 1-μm-thick layer with constant Ge content (50%). The SiGe alloy layers were grown in a chemical-vapor deposition (CVD) process on Si substrates. The surface of the pseudosubstrates were chemical-mechanically polished resulting in a root-mean-square (rms) roughness of approximately 0.2–0.3 Å. Prior to growth, the relaxed buffer layers were annealed in the molecular-beam epitaxy (MBE) system in order to remove the native oxide. No increase of the surface roughness was observed during this treatment.

On top of the pseudosubstrates, modulation-doped, strain-compensated multiple quantum wells (MQWs) were grown after depositing a 1000-Å-thick $Si_{0.5}Ge_{0.5}$ buffer layer. The symmetric MQWs grown at 300 °C and a growth rate of 0.5 Å/s consist of a $Si_{1-x}Ge_x$ layer with a very high Ge concentration ($0.7 \leq x \leq 0.85$) sandwiched between two nominally 12-Å-thick Si barriers. Depending on the Ge con-

[a]Electronic mail: thomas.fromherz@jku.at
[b]Present address: Institute of Condensed Matter Physics, Masaryk University, 611 37 Brno, Czech Republic.

 © 2005 American Institute of Physics

TABLE I. Nominal parameters of the samples LQW5–8. Since the structure of the samples is symmetric with respect to the middle of the QW, only half of the sample structure is listed.

Region			LQW5	LQW6	LQW7	LQW8
$Si_{0.5}Ge_{0.5}$ spacer	Undoped	(Å)	100	100	100	100
	Doped	(Å)	50	50	50	50
	Setback	(Å)	30	40	50	60
Si barrier		(Å)	12	12	12	12
$Si_{1-x}Ge_x$ well	Width	(Å)	60	48	40	34.2
	x		0.7	0.75	0.8	0.85
	Period	(Å)	440	452	464	478

tent, the QW width is designed in such a way that the equilibrium in-plane lattice constant of the layer stack consisting of the two Si barriers and the QW is matched to the lattice constant of the pseudosubstrate (strain compensation). Based on this design rule, QW widths between 34 and 60 Å result. The samples contain ten QWs separated by $Si_{0.5}Ge_{0.5}$ spacer layers with thicknesses in the range of 360–420 Å. They are *p*-type (boron) modulation doped on both sides of the QW to a level of 5×10^{17} cm^3. The 50-Å-thick doping layer is set back from the QW by 30–60-Å intrinsic $Si_{0.5}Ge_{0.5}$ layers. The whole MQW sample is sandwiched between 100-nm undoped and 10-nm-thick, *p*-type (boron, 5×10^{17} cm^3) top and bottom $Si_{0.5}Ge_{0.5}$ layers. The nominal sample parameters are summarized in Table I.

For polarization-dependent intersubband absorption measurements, the samples have been processed into 7-mm-long waveguides with facets polished at 45° with respect to the sample surface. The infrared radiation is coupled into the waveguide via one polished facet. Propagating through the waveguide, the radiation passes through the optically active MQW layers several times before it is coupled out via the opposite waveguide facet and detected by a HgCdTe detector. By this multipass geometry, the absorption features present in the transmission spectra of the MQW layers are enhanced. In addition, for this geometry the sample absorption can be measured both for transverse electric (TE) (electric-field vector of the radiation parallel to the MQW layers) and transverse magnetic (TM) (magnetic-field vector of the radiation parallel to the MQW layers) polarized radiation. The QWs are connected by alloyed Ohmic Al contacts. For modulating the carrier concentration in the QWs by an externally applied bias, top electrodes consisting of 50-nm Ti and 250-nm Al layers were evaporated on the sample surfaces.

III. EXPERIMENTAL RESULTS AND DISCUSSION

A. Structural analysis

The structural quality of the samples was determined by transmission electron microscopy (TEM) and x-ray scattering techniques. The TEM images reveal excellent structural quality with very sharp interfaces.[16] These experimental findings are further confirmed by the analysis of x-ray scattering measurements discussed in the following.

Two types of x-ray measurements, x-ray reflectivity (XRR) and x-ray diffraction (XRD), were performed on these samples. The XRR method is not sensitive to the crystalline quality of the sample but only to the refractive index and the interface roughness of the layers in the sample. In Fig. 1, the measured reflectivity as a function of the angle of incidence (α_i) of the x-ray beam [converted in reciprocal lattice coordinates Q_z according to $Q_z=(4\pi/\lambda)\sin(\alpha_i)$] is shown by the symbols for the samples LQW5–8. The data were obtained at the Swiss Synchrotron Light Source (SLS) at an x-ray wavelength of $\lambda=1.176$ Å.

The large number of sharp thickness fringes resulting from interferences of x-ray beams reflected at interfaces with a distance corresponding to the period of the MQW layer is an indication of the small surface roughness and the vanishing variations of the sample period. A more quantitative analysis of the sample structure was done by fitting the simulated XRR pattern to the experimental data as described in Ref. 17. The interface roughness responsible for the decrease of the average detector signal for increasing Q_z in Fig. 1 was included in the simulation by modifying the Fresnel coefficients of an ideal interface according to Ref. 18. The results

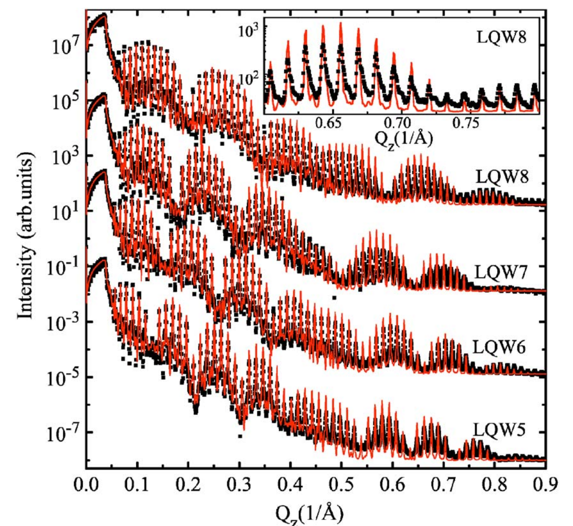

FIG. 1. (Color online). Measured (symbols) and simulated (lines) specular reflectivity patterns of the samples LQW5–8. For clarity, the traces are vertically offset for the various samples. In the inset, the XRR pattern for sample LQW8 is shown on an extended Q_z scale in order to highlight the details of the experimental and simulated data.

TABLE II. Layer thicknesses as extracted by fitting the simulated to the measured XRR traces (see Fig. 1). The estimated error is in the range of ±0.4 Å. For the Si barriers, the two values given in the table correspond to the thicknesses of the upper and lower barriers. The Ge content of the QWs is extracted from the XRD measurements (Ref. 16). The estimated error is in the range of ±0.005.

Region		LQW5	LQW6	LQW7	LQW8
$Si_{0.5}Ge_{0.5}$ spacer	(Å)	368.4	389.7	408.5	428.7
Si barrier	(Å)	14.1	12.9	14.3	13.7
	(Å)	13.1	14.3	13.5	13.5
$Si_{1-x}Ge_x$ well	(Å)	60.9	48.4	39.9	33.6
x		0.722	0.755	0.802	0.855
Period	(Å)	456.5	465.3	476.2	489.5

of the fits are shown by the full lines in Fig. 1. Excellent agreement between measurement and simulation was achieved over the whole range of angles for the structural parameters listed in Table II. We want to point out that the fitted parameters deviate only negligibly from the nominal parameters demonstrating the high degree of growth control achievable by state-of-the-art SiGe MBE.

From the fits, a rms interface roughness linearly increasing from 3 Å for the first interface to 3.6 Å for the last interface of the layer sequence was obtained. The lateral (vertical) correlation length Λ ($L_\perp$) of the interface roughness can be extracted from the profiles along the $Q_x(Q_z)$ direction of the horizontal sheets in the XRR map shown in Fig. 2(a). The Q_x profiles of two sheets at different Q_z values are plotted in more detail by the symbols in Fig. 2(b) for sample LQW8. In order to determine Λ, the experimental data were fitted to a model described in Refs. 19 and 20. The result of the fitting procedure is shown by the lines in Fig. 2. With the obtained values for Λ and $L_\perp$ given in the plot, the width of the x-ray signal in the Q_x direction is accurately described at different Q_z coordinates. The result for $L_\perp$ is larger than the total thickness of the MQW stack, thus indicating full correlation of all the interfaces of the MQW stack.

In order to determine the degree of strain compensation and the Ge content in the QWs, XRD measurements have been performed. These measurements show that the $Si_{1-x}Ge_x$ QWs and the Si barriers are pseudomorphically grown on the $Si_{0.5}Ge_{0.5}$ substrate and are alternately compressively and tensiley strained, so that the average stress (weighted by the layer thicknesses) of the QW layer sequences vanishes. A more detailed discussion of the results of the XRD measurements will be given elsewhere.[16] The values for the Ge concentration of the QWs listed in Table II were extracted from these measurements.

B. Intersubband absorption spectroscopy

Absorption measurements were performed by modulating the sample transmission by a square-wave voltage (typically −2−0.5 V, frequency of ~70 kHz) applied between the Ohmic contacts and the top electrodes and detecting the resulting change in transmission via lock-in techniques. The

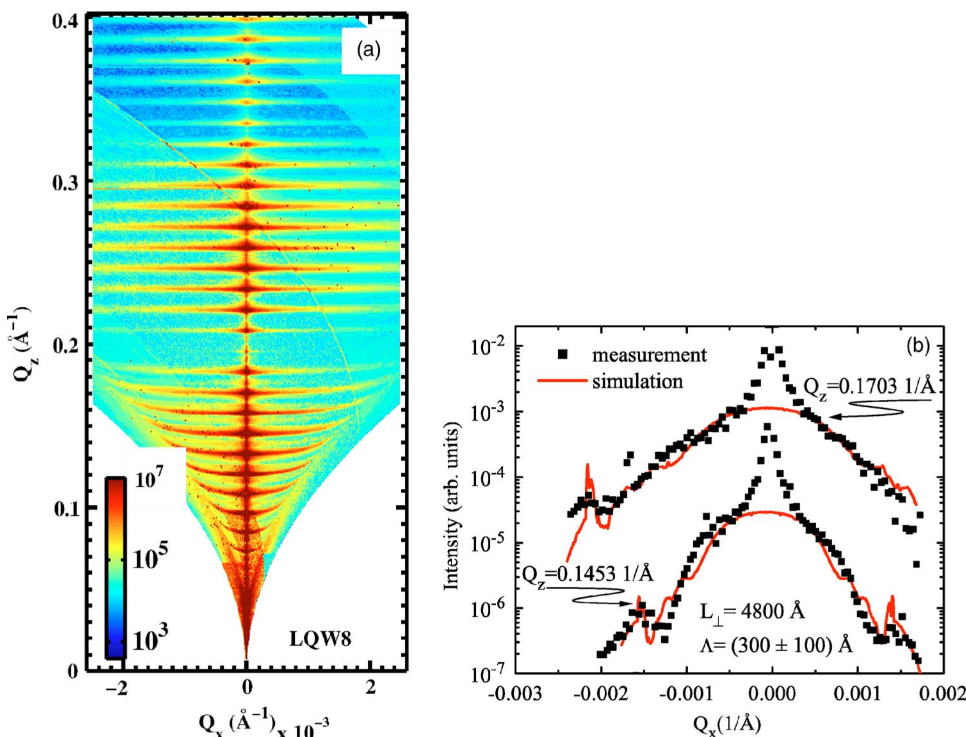

FIG. 2. (Color online). Dependence of the XRR signal measured for LQW8 on the scattering wave vector in the Q_x, Q_z plane, where the Q_z direction is perpendicular to the sample surface. (a) XRR map. (b) The experimental data (symbols) were obtained by cross sections through the map shown in (a) at the Q_z coordinates indicated in (b). For clarity, the data corresponding to different Q_z are offset vertically. The full lines result from fitting the experimental data to the model described in Ref. 19.

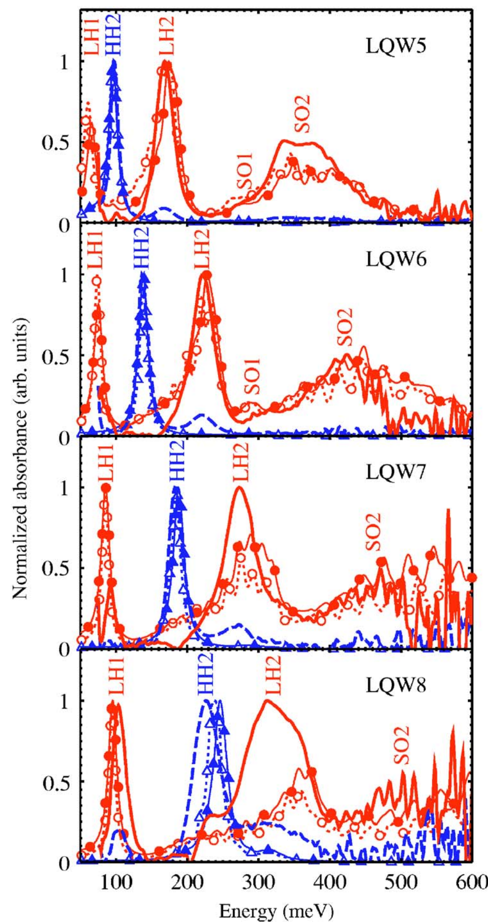

FIG. 3. (Color online). Measured (bold lines) and calculated (lines with superimposed symbols) polarization-dependent intersubband absorption spectra for a temperature of $T=15$ K. The spectra measured for TE (TM) polarization are shown by the full (broken) lines. The results calculated for radiation with electric field parallel to the (x,y) plane (z direction) are shown by the lines with superimposed circles (triangles), where z denotes the growth direction. The full symbols indicate the results obtained using the structural parameters listed in Table I, whereas the open symbols represent the results based on the nominal sample parameters. (Note that in the waveguide geometry employed in the experiment, the TM polarization contains both x,y and z polarizations.) For normalization, the absorption spectra calculated for x,y polarization were multiplied by a factor of ~ 6.2 times larger than the spectra for z polarization.

spectral dependence of the transmission changes was obtained by feeding the lock-in signal into a Fourier transform spectrometer operated in a step-scan mode.

Figure 3 shows the normalized results of the transmission measurements for TE- (bold full lines) and TM- (bold broken lines) polarized radiation for the samples LQW5–8 at a temperature of 15 K. The observed absorption spectra show a rich peak structure that strongly depends on the direction of the polarization of the infrared radiation.

In order to determine the origin of all intersubband transitions contributing to the sample absorbance, six-band $\mathbf{k}\cdot\mathbf{p}$ envelope function calculations of the energy spectra of the valence-band QWs have been performed. These calculations are based on a strain-dependent Luttinger-Kohn Hamiltonian that includes the heavy-hole (HH), light-hole (LH), and spin split-off (SO) valence bands and their mutual coupling due to strain and hole in-plane momentum. The details of the calculations are given in Ref. 21. However, since the interpolation scheme[22] for the Luttinger parameters γ_{1-3} used in Ref. 21 becomes inaccurate for large Ge fractions, in this work the interpolation scheme suggested in Ref. 23 was used. In Fig. 4 these band parameters are plotted versus the Ge content of the epitaxial layer: in Fig. 4(a) the energetic positions of the HH, LH, and SO valence bands for a $Si_{1-x}Ge_x$ layer on a $Si_{0.5}Ge_{0.5}$ substrate are shown, whereas Fig. 4(b) depicts the Luttinger parameters.

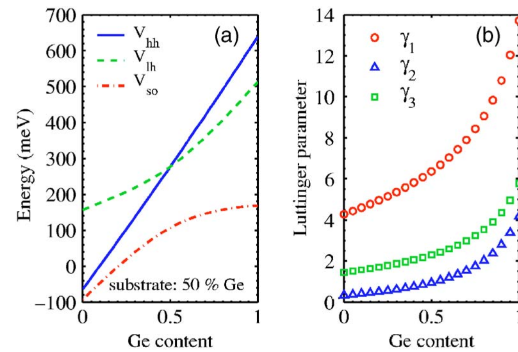

FIG. 4. (Color online). Band-structure parameters used in this work: (a) Energetic position of the HH, LH, and SO valence band edges for a $Si_{1-x}Ge_x$ layer grown on a $Si_{0.5}Ge_{0.5}$ substrate calculated according to Ref. 21 and references therein. The origin of the energy axis corresponds to the average of the HH, LH, and SO valence band edges in bulk Si. (b) Luttinger parameters as function of the Ge concentration obtained according to the interpolation scheme suggested in Ref. 23 and references therein.

Both the structural parameters determined by the x-ray experiments and the nominal parameters have been used as input parameters for the calculations. Hence, the only fitting parameter that enters the simulation is the broadening of the transition energy which was assumed to be 14 meV full width at half maximum (FWHM).

The absorption spectra calculated for $T=15$ K are plotted in Fig. 3 for the samples LQW5–8 with thin lines and superimposed symbols, where the circles and triangles indicate the results for radiation with the electric-field vector perpendicular (x,y) and parallel (z) to the growth direction, respectively. The full symbols indicate the results obtained using the parameters determined by x-ray experiments (Table II), whereas the lines with the open symbols are based on the nominal parameters (Table I). For both set of parameters, the differences between the simulated spectra are insignificant and excellent agreement between the calculated and measured absorbance spectra is achieved for all samples. (While comparing the simulated and measured absorption spectra, one has to keep in mind that due to the waveguide geometry employed in the experiment the TM-polarized radiation contains both x, y, and z components of the electric field. The influence of the waveguide on the observed absorption lines will be discussed in one of the following paragraphs.) As the same lifetime broadening was assumed for all transitions and all samples, the different line shapes of the simulated absorption peaks shown in Fig. 3 are caused by the different in-plane dispersions of ground and excited states as well as by the coupling of the excited states to the continuum. From the comparison with the measured spectra, it is evident that these effects dominate the observed line shapes. A detailed analysis of the broadening mechanisms resulting in a 14-meV

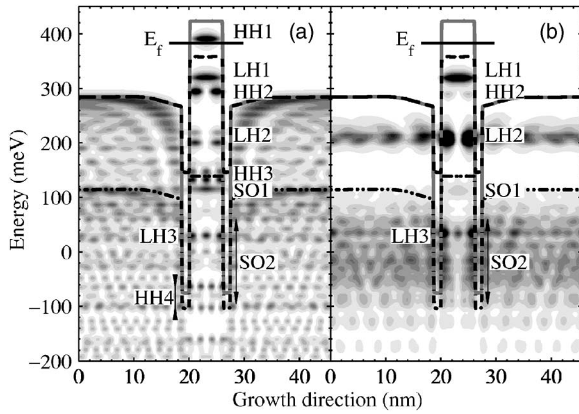

FIG. 5. (a) Contour plot of the hole distribution probability density calculated for LQW5 at the Γ point. (b) Contour plot of the hole distribution probability integrated over the in-plane and perpendicular wave vectors and weighted by the modulus of the transition matrix element for x,y polarization from the HH1 ground state to the respective final state. In (a) and (b) the contour plot is gray-scale coded with black (white) indicating maximum (zero) probability. The spatial profiles of the HH, LH, and SO valence bands are shown by the full gray, dashed, and dashed-dotted black lines, respectively. The horizontal line labeled E_f indicates the Fermi energy calculated for $T=15$ K. The origin of the energy axis corresponds to the average of the HH, LH, and SO valence band edges in bulk Si.

linewidth used in the simulations is beyond the scope of this paper. However, in analogy to recent results obtained on similar samples,[24,25] we assume that interface roughness scattering is the process that determines the linewidth and that subtle many-particle interactions that have been identified to determine the absorption line shapes in high-quality III-V QWs (Refs. 26 and 27) are dominated by this process.

The best agreement between the calculated and measured absorbance is achieved for the the samples containing the broader QWs. In Fig. 3 the peaks are labeled according to the main character of the final states of the transition. As an example, the band structure of LQW5 is shown in Fig. 5(a) for vanishing in-plane and perpendicular wave vector components together with a contour plot of the distribution probability (i.e., the squared moduli of the wave functions). The probability of finding a hole at a certain energy and position is broadened along the energy axis in Fig. 5 by half the linewidth used for calculating the absorption spectra and is gray-scale coded with white and black indicating vanishing and maximum probabilities, respectively. The full gray, the black-dashed, and dashed-dotted lines represent the band-edge profiles of the HH, LH, and SO valence bands, respectively, whereas the straight line labeled E_f indicates the Fermi energy calculated for 15 K. At this temperature, only the ground state (labeled HH1 in Fig. 5) is occupied by holes for all samples investigated in this work.

The identification of the HH states is unambiguously possible, since at $k_{\text{in plane}}=0$ the HH states are decoupled from the LH and SO bands and coupling occurs only at finite in-plane wave vector. However, due to the confinement and the strain, which couples the LH and SO states also at $k_{\text{in plane}}=0$, the identification of these states is not as straight forward as for the HH states. For example, the states shown at 115 and −17 meV in Fig. 5(a) (labeled SO1 and SO2) are 33% LH and 67% SO and 27% LH and 73% SO mixtures, respectively. Whereas for these states, there is a clearly dominating contribution that allows an identification, this is not the case, for example, for the state at 30 meV (labeled LH3) which is a 56% LH and 44% SO mixture. However, the labeling in Fig. 5(a) seems to be consistent for the following reasons: The energy of this state is between the energy of the SO1 and SO2 states; its dispersion along the [100] direction shows a negative effective mass, which is not possible for SO states; the transition matrix element to the HH1 ground state vanishes for (x,y)-polarized radiation at $k_{\text{in plane}}=0$.

Figure 5(b) shows for the same sample a contour plot of the distribution probability of those states, in that a hole from the ground state (HH1) can be excited by light in x,y polarization. In the plot, the distribution probability is weighted by the transition matrix element from the ground state and is integrated over the in-plane and perpendicular wave vector. The integration over the perpendicular wave vector is mandatory since most of the excited states are coupled to the continuum and, therefore, exhibit both a miniband and a matrix element dispersion for this wave-vector direction.

Figure 5(b) shows that the absorption to the continuum is dominated by states with only one minimum in the distribution probability occurring at the center of the QW with energies between −100 and 100 meV. In this energy range, these states are predominantly built up from the SO band, since the HH2 and LH2 occur at much larger energies. The transitions from the HH1 ground state to the SO2 are allowed also at $k_{\text{in plane}}=0$ for (x,y)-polarized radiation.[21] Thus, they are the dominating transitions to the continuum states as shown in Figs. 3 and 5(b).

In order to include the effects of the experimental waveguide geometry in our simulations, we have calculated the dielectric function of the QWs from the absorption spectra shown in Fig. 3 by a Kramers-Kronig transformation. The dielectric function was then used to model the QW region of the sample that is described as a dielectric stack consisting of a Si substrate, bottom contact, QW sequence, top contact, and Al top electrode. The transmission through the waveguide was simulated by the transfer-matrix method.[28] Figure 6 shows the simulated waveguide transmission spectra (thin lines with symbols) together with the experimental data (bold lines) for the samples LQW5 [panels (a) and (b)] and LQW8 [panels (c) and (d)]. Two different assumptions for the influence of the externally applied voltage on the sample absorption have been considered: (i) for the result shown by the thin lines with open circles it is assumed that the topmost QW is completely depleted from holes by the applied bias, whereas the lines with filled squares are obtained by assuming (ii) that the hole concentration in all ten QWs is modified equally by the applied bias. For assumption (i), using the doping profile and the structural parameters it is readily calculated that only the top QW can be depleted by the voltages used in the experiment, resulting in a 10% modulation of the total sample absorbance due to the QWs. Figure 6(b) shows that at the energy of the HH1→HH2 transition (at ~100 meV) a modulation of 2% of the total waveguide transmission is observed for LQW5. According to assumption (i), the observed transmission change is due to the deple-

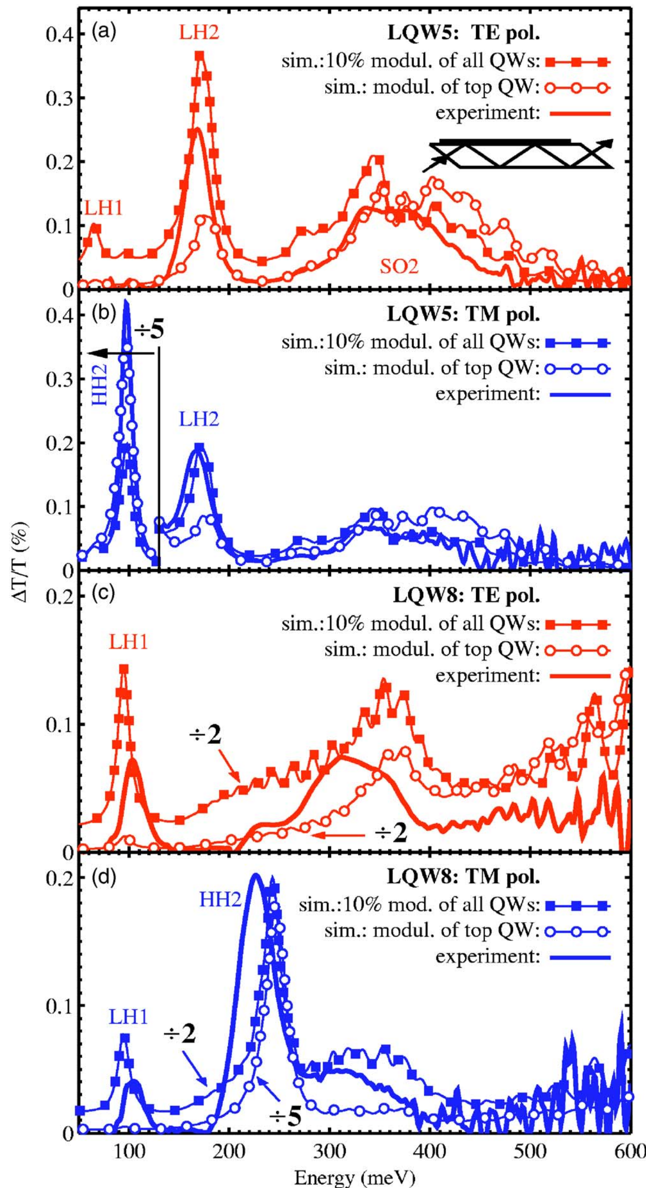

FIG. 6. (Color online). Low-temperature ($T=15$ K) measured (bold lines) and simulated (thin lines with superimposed symbols) waveguide absorption spectra for TE and TM polarizations. The simulation is based on the transfer-matrix method (Ref. 28). The lines with filled squares were obtained by assuming a bias-induced 10% modulation of the hole concentration in *all* ten QWs, whereas the lines with open circles result from assuming a complete hole depletion from the *topmost* QW only.

tion of only one QW, thus a total absorption of 20% for all ten QWs can be estimated for this sample. This estimation is in good agreement with the total HH1→HH2 absorbance as obtained from the ratio of TM- and TE-polarized waveguide transmission measured at a 0-V bias (23%) (Ref. 29) and with the simulation of the total TM-polarized waveguide absorption at the HH1→HH2 transition (20%) for LQW5.

For assumption (i), the results were obtained by calculating the difference between the transmission of a waveguide containing a stack of ten doped QWs and of one containing only nine doped and one (the topmost) undoped QW. As a consequence of assumption (i), the simulated TE-polarized absorption lines are strongly suppressed for the transitions at low energies. As discussed, for example, in Ref. 21 the suppression results from the boundary conditions for the reflection of the TE-polarized radiation at the metal gate requiring a vanishing field amplitude close (on the scale of the wavelength) to the metal surface for this polarization. The suppression due to assumption (i) becomes most evident for the simulated transmission spectra of LQW8 shown by the line with open circles in Fig. 6(c). In this plot, the HH1→LH1 absorption at ~100 meV is nearly completely absent, whereas in the experimental spectra significant absorption is observed at this wavelength. Also the HH1→LH2 transition of LQW5 simulated under assumption (i) shown at ~175 meV in Fig. 6(a) is too weak as compared to the simulated HH1→SO2 band between 300 and 500 meV and to the measured absorption.

In order to further highlight the dominating influence of the metal gate on the sample absorbance, the waveguide absorption was also simulated for assumption (ii). In order to get comparable results for assumptions (i) and (ii), a 10% depletion of the hole concentration for all QWs was assumed for (ii). It is interesting to note that for the samples investigated in this work a depletion of 10% of holes in all QWs (i.e., a net sheet concentration of 5×10^{10}-cm^{-2} negatively charged acceptors) corresponds to a space-charge region extending over all ten QWs at a 2-V bias. For this reduced hole concentration, an absorption spectrum was calculated from the $\mathbf{k}\cdot\mathbf{p}$ band structure by reducing the Fermi energy accordingly. With this new absorption spectrum, the waveguide transmission was simulated as outlined in the preceding paragraphs. The differences to the transmission spectra simulated for the undepleted samples are shown in Fig. 6 by the thin lines with filled squares. As shown in Fig. 6, for assumption (ii) all the peaks observed in the experiment are also present in the simulation of the modulated waveguide transmission spectra, indicating that assumption (ii) results in a qualitatively better agreement between experiment and simulation. However, the peak heights observed in the TE-polarized transmission-change spectrum for LQW8 are approximately four times smaller than the simulated ones, while for LQW5 a reasonable agreement up to a factor of ~1.5 was obtained. While the larger overall deviation of experiment and simulation for LQW8 might be due to less efficient hole modulation in sample LQW8 as compared to LQW5, a systematic underestimation of the TM-polarized HH1→HH2 transmission change by a factor of ~2 relative to the TM-polarized transmission change at the energies of the HH1→LH1 and of the HH1→LH2 transitions in the samples LQW8 and LQW5, respectively, is evident in the simulated transmission spectra. As shown in Fig. 3, the LH transitions can only be excited by an electric radiation field component parallel to the (x,y) plane. Thus, they are present in the TM-polarized waveguide transmission spectrum due to (x,y) electrical-field component, whereas the HH transitions are excited by the z component of the TM-polarized radiation. Since the z component of the electric field of the radiation exhibits an antinode upon reflection on a metal surface resulting in a *maximum* of the energy density close to the metal surface, the simulated HH transitions show an opposite behavior than the LH transition with respect to assumptions (i) and (ii): Figures 6(b) and 6(d) show that the simulated

modulation of the waveguide transmission at the HH1 $\rightarrow$HH2 transition energies is *smaller* for assumption (ii) than for assumption (i). Thus, in order to understand the measured waveguide transmission change for both directions of polarization, a hole modulation profile in between the two profiles represented by assumptions (i) and (ii) has to be assumed, with a larger modulation of the hole concentration in the top QW and a smaller but still significant modulation in the QWs closest to the substrate. Consequently, a modulation of the hole concentration in the topmost QW *only* can be ruled out.[30]

As shown in Fig. 6 the simulated modulation of waveguide transmission critically depends on assumptions that have to be made to describe the experiment. In addition to the modulation depth profile, also the conductivity parallel to the QW layers has to be taken into account since it results in two-dimensional free-carrier absorption in analogy to the Drude absorption in three dimensions. In the simulation of the TE waveguide transmission, this absorption appears as a slowly varying background for energies below $\sim$150 meV in Figs. 6(a) and 6(c). The strength of this absorption depends on the sheet carrier concentration, as well as the in-plane mobility that were set to $5\times10^{11}\,\text{cm}^2/\text{period}$ and $1000\,\text{cm}^2/\text{V s}$, respectively, for all samples.

The discussion of Fig. 6 shows that by taking into account the experimental waveguide geometry a more detailed information about the relative strengths of the various absorption lines can be extracted from the measured spectra. However, more parameters enter these simulations and, thus, an interpretation is not as straight forward as the direct comparison of experimental transmission and calculated absorption spectra shown in Fig. 3 for which only one parameter (the transition linewidth) is required.

IV. SUMMARY

In this work we have shown that high-quality strain-compensated SiGe QWs with high Ge content in the wells can be grown on $Si_{0.5}Ge_{0.5}$ pseudosubstrates by state-of-the-art low-temperature MBE. Structural analyses by XRD, XRR, and TEM revealed an almost perfect match of actual and designed structural parameters. As evidenced by intersubband absorption spectroscopy, based on the structural parameters the *band structure* of these QWs can be modeled very accurately by a six-band $\mathbf{k}\cdot\mathbf{p}$ envelope function approach without any fitting parameters. The only fitting parameter used in this work is related to the broadening of intersubband *transitions*. However, except for the HH1 $\rightarrow$HH2 transition in the wider QWs, in that the HH2 state is still well confined, this fitting parameter has only minor influence on the general shape of the calculated absorption lines, since for the samples investigated in this work the dominating broadening mechanisms are differences in the in-plan dispersions of ground and excited states as well as coupling of the excited QW states to the continuum of states in the $Si_{0.5}Ge_{0.5}$ spacer layers separating adjacent QWs. The small residual deviations of actual and designed structural parameters result in negligible differences between the designed and the actual band structure. Thus, applying the well-calibrated model calculations as a design tool together with the superior MBE growth process will allow us to reliably engineer and optimize the band structure of more complicated QW sequences as required, for example, for SiGe-based quantum cascade emitters.

ACKNOWLEDGMENTS

This work was supported by the EC under the project "SHINE" (IST-2001-38035), by the Ministry of Education of Czech Republic under Project No. MSM 0021622410, and by the Grant Agency of Czech Republic under Project No. 202/05/P286. We would like to thank STMicroelectronics for supplying the SiGe pseudosubstrates. The assistance of the beamline scientists B. Schmidt and B. Patterson from MS-SLS is gratefully acknowledged.

[1] For a review see: K. Brunner, Rep. Prog. Phys. **65**, 27 (2002).
[2] W. L. Ng, M. A. Lourenço, R. M. Gwilliam, S. Ledain, G. Shao, and K. P. Homewood, Nature (London) **410**, 192 (2001).
[3] J. M. Sun, T. Dekorsy, W. Skorupa, B. Schmidt, A. Mücklich, and M. Helm, Phys. Rev. B **70**, 155316 (2004).
[4] V. Lehmann and U. Gösele, Appl. Phys. Lett. **58**, 856 (1991).
[5] B. Gelloz, T. Nakagawa, and N. Koshida, Appl. Phys. Lett. **73**, 2021 (1998).
[6] S. Chan and P. Fauchet, Appl. Phys. Lett. **75**, 274 (1999).
[7] L. Pavesi, L. D. Negro, C. Mazzoleni, G. Franzò, and F. Priolo, Nature (London) **408**, 440 (2000).
[8] L. Rebohle, J. von Borany, H. Fröb, and W. Skorupa, Appl. Phys. B: Lasers Opt. **71**, 131 (2000).
[9] P. Kruck, M. Helm, T. Fromherz, G. Bauer, J. Nützel, and G. Abstreiter, Appl. Phys. Lett. **69**, 3372 (1996).
[10] P. Rauter, T. Fromherz, G. Bauer, L. Diehl, G. Dehlinger, H. Sigg, D. Grützmacher, and H. Schneider, Appl. Phys. Lett. **83**, 3879 (2003).
[11] G. Dehlinger, L. Diehl, U. Gennser, H. Sigg, J. Faist, K. Ensslin, D. Grützmacher, and E. Müller, Science **290**, 2277 (2000).
[12] L. Diehl *et al.*, Appl. Phys. Lett. **81**, 4700 (2002).
[13] I. Bormann, K. Brunner, S. Hackenbuchner, G. Zandler, G. Abstreiter, S. Schmult, and W. Wegscheider, Appl. Phys. Lett. **80**, 2260 (2002).
[14] S. Lynch *et al.*, Appl. Phys. Lett. **81**, 1543 (2002).
[15] R. Bates *et al.*, Appl. Phys. Lett. **83**, 4092 (2003).
[16] C. Falub *et al.*, J. Cryst. Growth **278**, 495 (2005).
[17] T. Roch *et al.*, J. Appl. Phys. **91**, 8974 (2002).
[18] P. Croce and L. Nevot, Rev. Phys. Appl. **11**, 113 (1976).
[19] V. Holý and T. Baumbach, Phys. Rev. B **49**, 10668 (1994).
[20] In these fits, the parameter *h* describing the fractal dimension of the interfaces was set to 0.5.
[21] T. Fromherz, E. Koppensteiner, M. Helm, G. Bauer, J. Nützel, and G. Abstreiter, Phys. Rev. B **50**, 15073 (1994).
[22] M. M. Rieger and P. Vogl, Phys. Rev. B **48**, 14276 (1993).
[23] R. Winkler, M. Merkler, T. Darnhofer, and U. Rössler, Phys. Rev. B **53**, 10858 (1996).
[24] S. Tsujino *et al.*, Appl. Phys. Lett. **84**, 2829 (2004).
[25] S. Tsujino *et al.*, Appl. Phys. Lett. **86**, 062113 (2005).
[26] J. Li and C. Z. Ning, Phys. Rev. B **70**, 125309 (2004).
[27] I. Waldmüller *et al.*, Phys. Rev. B **69**, 205307 (2004).
[28] See, for example, B. Harbecke, Appl. Phys. B: Photophys. Laser Chem. **39**, 165 (1986).
[29] S. Tsujino and H. Sigg (unpublished).
[30] Assuming a voltage-independent depletion of the first QW by the top metal contact and a voltage-dependent modulation of the hole concentration in the next but one QW can also be ruled out, since for this assumption similar results with a complete suppression of the LH1 absorption for LQW8 is obtained within our model.